Engineering Structures 306 (2024) 117680

Contents lists available at ScienceDirect

Engineering Structures

journal homepage: www.elsevier.com/locate/engstruct

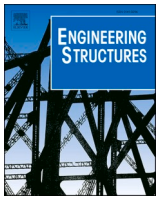

Investigation on the elastic flexural stiffness of dot-by-dot wire-and-arc additively manufactured stainless steel bars

Vittoria Laghi [1], Valentina Alena Girelli, Giada Gasparini, Tomaso Trombetti, Michele Palermo [*]

Department of Civil, Chemical, Environmental and Materials Engineering (DICAM) - University of Bologna, Viale del Risorgimento, 2, 40136 Bologna, Italy

ARTICLE INFO

Keywords:
Directed energy deposition
Stainless steel
Experimental tests
Three-point bending
Flexural stiffness
Numerical simulations
dot-by-dot deposition strategy

ABSTRACT

Among different metal additive manufacturing (AM) technologies, arc-based Directed Energy Deposition, also known as Wire-and-Arc Additive Manufacturing (WAAM), is considered the most suitable for large-scale structural components production. In particular, the WAAM printing strategy referred to as "dot-by-dot" allows the realization of complex 3D lattice forms at the scale of structural steel parts, composed of unitary cells made of slender bars. Nonetheless, the outcomes of this process are still to be properly investigated in terms of their mechanical behavior under various loading conditions. To assess the buckling behavior of WAAM-produced slender bars, extensive effort is requested to properly characterize the main driving aspects, namely the flexural stiffness possibly influenced by mechanical anisotropy induced by the printing process and the influence of the geometrical imperfections. The present work reports the first results of experimental bending tests conducted on vertically printed (i.e. with a fixed build angle equal to 0°) straight dot-by-dot WAAM stainless steel bars, as an initial investigation towards a more comprehensive analysis of the buckling behavior of WAAM slender elements. The results are then interpreted by introducing three approaches of increasing complexity, including two analytical approaches based on a simplified idealization of the real geometry of the bar, and a third approach based on the reconstruction of the real geometry of the bar using advanced numerical simulations and 3D scanning. The three approaches lead to a different appraisal of the influence of the geometrical irregularities on the flexural stiffness of the specimens. The main results of the present study could be utilized to interpret the results of future experimental compressive tests on WAAM slender elements and to develop ad-hoc buckling curves for structural design purposes.

1. Introduction

Wire-and-Arc Additive Manufacturing (WAAM) is an arc-based metal 3D printing technique suitable to realize large-scale structural components for construction applications [1–3]. Regarding steel alloys, in the last few years various research studies focused on the microstructural, geometrical and mechanical features of the printed parts. Up to now, two different printing strategies have been explored to realize WAAM structural elements: (i) the so-called layer-by-layer deposition strategy to realize shell and planar elements [4–8] and (ii) the so-called dot--by-dot (or point-by-point) deposition strategy to realize bars and lattice structures (Fig. 1) [9–12]. Intense research work has been devoted over the last decade in characterizing large-scale metal structures fabricated with WAAM technology [3,13,14]. Among others, the research group from Imperial College London has carried out an extensive experimental and analytical investigation on the mechanical properties of WAAM-produced steel members and joints for structural applications [15–21]. Recently, the research group from TU Darmstadt has applied WAAM for structural applications, including novel connection systems [22,23] and a demonstrator for a bridge [24].

Dot-by-dot WAAM bars are characterized by the following features which should be properly investigated: (i) different material properties with respect to the conventional wrought part [25]; (ii) geometrical irregularities related to the specific deposition strategy (in terms of lack of straightness and variation of the cross-section) [26]; (iii) possible influence of the process parameters, deposition strategy, build and nozzle angles on the mechanical response [27]. Hence, specific considerations on both geometrical and mechanical features of the as-built printed bars

* Corresponding author.
E-mail address: michele.palermo7@unibo.it (M. Palermo).
[1] ORCiD ID: https://orcid.org/0000-0001-8395-21942

https://doi.org/10.1016/j.engstruct.2024.117680
Received 31 May 2023; Received in revised form 8 February 2024; Accepted 13 February 2024
Available online 8 March 2024

Fig. 1. WAAM dot-by-dot technique [31].

should be addressed. The research group from ETH Zurich has developed a novel fabrication study for hybrid joints via point-by-point (or dot-by-dot) WAAM strategy and tested dot-by-dot bars through tensile and compression tests on bars of different slenderness [27,28]. More recently, the research groups at TU Munich and TU Braunschweig have carried out research on applying WAAM as reinforcement for concrete structures [29,30].

Over the years, the authors have been studying the mechanical response of WAAM-produced parts for structural design applications [10,32,33]. With specific focus on WAAM bars, an extensive experimental investigation was planned to assess the mechanical response of stainless-steel printed bars under tension, bending and compression. The aim was twofold: (i) to investigate the influence of the geometrical irregularities proper of the printing process on the mechanical response of the printed bars; (ii) to evaluate the structural behavior under different applied external forces, such as tension, compression and bending. In [26] the mechanical response in tension of single bars printed at three different build angles was investigated. The results showed a detrimental effect of increasing build angles on the geometrical irregularities, which also affected the key effective mechanical parameters.

The present study aims at assessing the mechanical response of straight dot-by-dot WAAM bars printed vertically (i.e. with a constant build angle equal to 0°) under bending-induced internal forces through experimental methods (geometrical characterization and three-point bending tests), analytical investigations and numerical simulations. The main novel aspect of the research is the assessment of the elastic flexural rigidity of the bar which, apart from being the main parameter governing the flexural deformability of the bars, is also the key parameter governing their buckling behavior. Generally speaking, the elastic flexural behavior of the bars can be influenced by the geometrical irregularities and the mechanical anisotropy of the WAAM stainless steel induced by the markedly oriented microstructure (see e.g. [4,34–36]) resulting from the deposition strategy. The results in terms of flexural rigidity and geometrical imperfections could be of fundamental importance to properly interpret the buckling behavior of slender WAAM bars and calibrate ad-hoc buckling curves for structural design purposes.

The paper is organized as follows. Section 2 provides the problem formulation in terms of the design issues of dot-by-dot WAAM bars with specific focus on the evaluation of their elastic flexural behavior. Then three approaches are introduced to assess the elastic flexural stiffness of WAAM bars from geometrical characterization and mechanical tests. Section 3 presents the experimental methods adopted to fabricate and characterize the dot-by-dot WAAM bars, while Section 4 illustrates the Finite Element Analysis (FEA) developed to assess the flexural mechanical response of WAAM bars. Section 5 illustrates the main results obtained from the geometrical characterization, three-point bending tests and FEA developed to calibrate the material flexural elastic modulus of the tested specimens considering the imported 3D-scanned geometry. Some discussions and conclusions are finally drawn.

2. Problem formulation

2.1. Design issues for dot-by-dot WAAM bars

The dot-by-dot printing strategy consists in a spot-like deposition strategy, whose outcomes are usually metal bars suitable to realize different types of structures including gridshells and lattice elements. As for WAAM planar elements realized with layer-by-layer deposition strategy, also dot-by-dot WAAM bars are characterized by some peculiar aspects which substantially differ from the conventional material. In detail, the following features should be considered: (i) influence of the build and nozzle angles; (ii) inherent geometrical irregularities of the investigated WAAM process, in terms of non-uniform circular cross-section and out of straightness of the longitudinal axis; (iii) non-uniform mechanical properties along the length of the bar depending on the deposition strategy and (iv) possible mechanical anisotropy depending on the microstructure induced by the printing process and deposition strategy. Fig. 2 provides a graphical representation of the main features reported above as emerged from the results of previous tensile tests [26].

Therefore, as a consequence of all the above mentioned issues, dot-by-dot WAAM bars could manifest, even for a fixed set of process parameters and for a fixed build angle, elastic and inelastic properties (Young's moduli and Poisson's ratios, yield and ultimate strengths and deformations) that may vary with the type of applied loads and resulting internal forces (e.g. axial tension/compression, bending, shear, torsion). The large variability of such properties can be related to low repeatability of the process at either the scale of the entire batch production (leading to specimen-to-specimen variability) or at the scale of the single specimen production (leading to local inherent variability). Therefore, adequate geometrical and mechanical models are necessary to capture both the overall specimen-to-specimen variability and the local inherent variability of single specimens.

A typical dot-by-dot WAAM bar is characterized by one main building direction (corresponding to the bar longitudinal axis z) and a nominal constant cross-section corresponding to the dimension of the weld drop. Hence, its ideal digital model used as input in the printing process corresponds to a straight bar having constant circular cross-section (Fig. 3a). The geometry of the ideal model is therefore described by the nominal bar length (L_n), the nominal cross-sectional diameter (d_n) and the corresponding nominal moment of inertia (J_n). On the other hand, the real printed outcome is characterized by: (i) a non-uniform circular cross-section with continuously variable diameter $d_{real}=d_{real}(z)$ leading to a continuously variable moment of inertia $J_{real}=J_{real}(z)$, (ii) a non-perfectly straight longitudinal axis (formed by the polyline connecting the centroids of each circular cross-section $C_{real} = C_{real}(z)$, Fig. 3c).

For structural design purposes, a simplified approach could be adopted to model the bar geometry at the scale of an entire batch production. It is based on the use of effective geometrical parameters associated to a perfectly cylindrical bar having the same volume of the real bar, thus resulting in a uniform (or effective) diameter (d_{eff}) and moment of inertia (J_{eff}) along the bar length (Fig. 3b). Therefore, the mechanical response of WAAM parts can be evaluated considering this effective geometrical model. This approach was already employed to characterize batches of both planar coupons [4,6,37] and dot-by-dot bars [26] subjected to tensile loading.

2.2. The proposed approaches to evaluate the flexural stiffness of dot-by-dot WAAM bars

A simply supported dot-by-dot WAAM bar of nominal diameter d_n and nominal length L_n subjected to a concentrated load F is here investigated. From the considerations drawn in Section 2.1 it is clear that the flexural rigidity of the bar R, defined as the product of the flexural Young's modulus E_f and moment of inertia J, may continuously

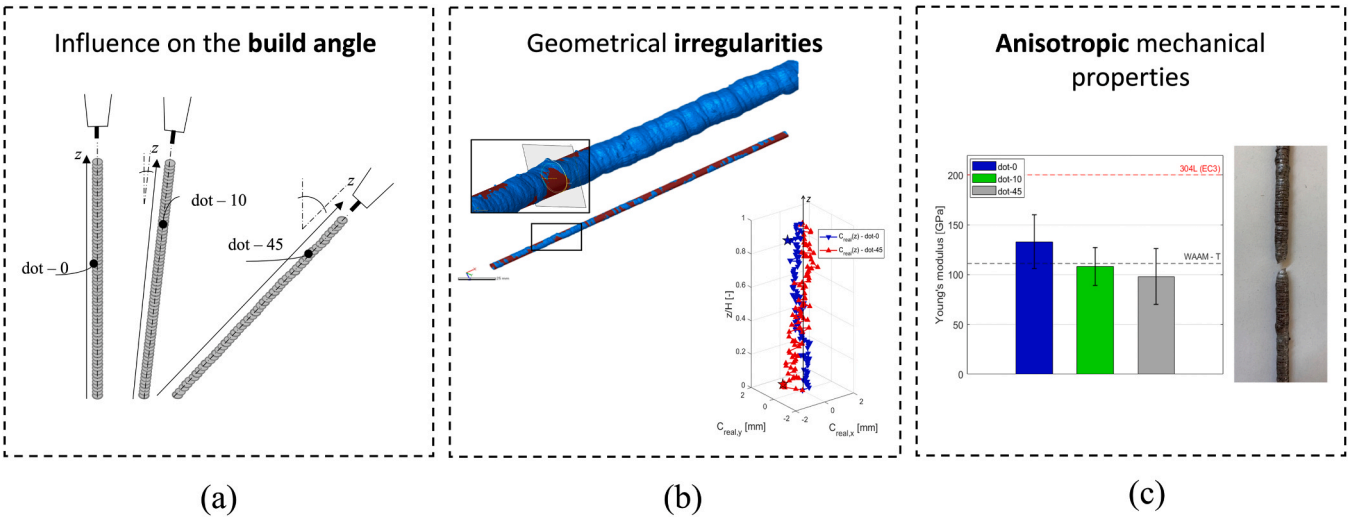

Fig. 2. Design issues for WAAM bars: (a) influence of the build angle and nozzle angle; (b) geometrical irregularities as obtained from 3D laser scanning; (c) variation of the Young's modulus with build direction as obtained from tensile tests.
Adapted from [26].

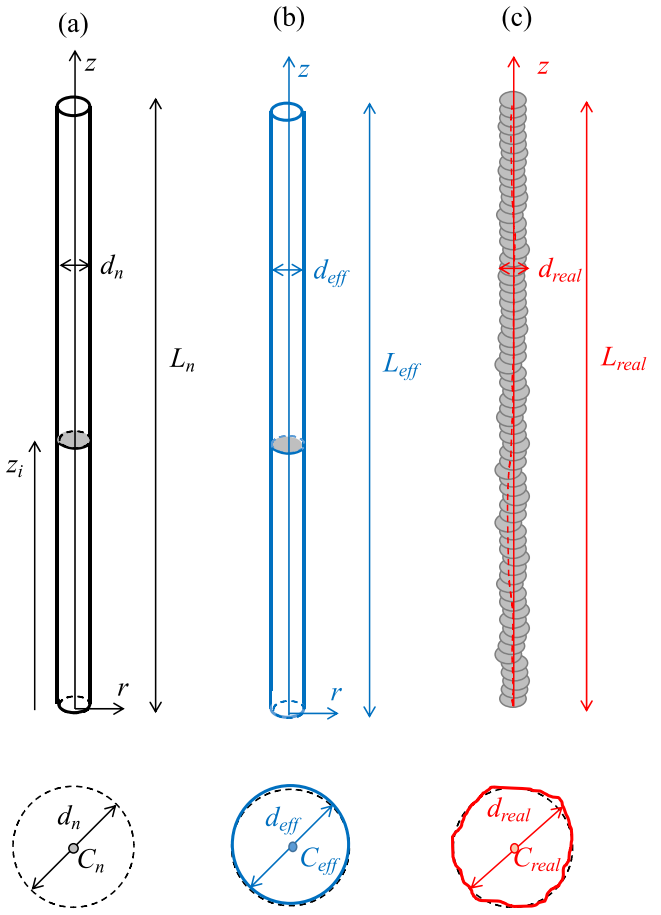

Fig. 3. WAAM bar: (a) digital input model; (b) effective geometry; (c) real geometry.

vary along the bar length and should, therefore, be considered a function of z, i.e $R(z) = E_f(z)J(z)$. From basic principles of structural mechanics, the vertical elastic displacement at the mid-span δ can be evaluated by making use of the principle of virtual works (ignoring the contribution due to the shear deformability, typically negligible for compact cross sections) according to the following integral form [38]:

$$\delta = \int_0^L \frac{M \cdot M'}{E_f J} dz \tag{1}$$

where:

$$M = \begin{cases} F \cdot \frac{z}{2} & for\ 0 \le z \le l/2 \\ F \cdot \left(\frac{l-z}{2}\right) & for\ l/2 \le z \le l \end{cases} \tag{2}$$

$$M' = \begin{cases} 1 \cdot \frac{z}{2} & for\ 0 \le z \le l/2 \\ 1 \cdot \left(\frac{l-z}{2}\right) & for\ l/2 \le z \le l \end{cases} \tag{3}$$

M is the real bending moment at the generic cross-section z due to the applied vertical load F. M' is the virtual bending moment at the generic cross-section z due to a unitary virtual vertical load applied at the mid-span cross-section (Fig. 4a).

For the case of a linear elastic homogeneous cylindrical bar with constant along-the-length flexural stiffness, Eq. 1 simplifies as follows [38]:

$$\delta = F \frac{L^3}{48 E_f J} \tag{4}$$

The quantity in Eq. 4 relating the external force F with the mid-span vertical displacement δ, i.e., $\frac{48E_fJ}{L^3}$, represents the vertical translational stiffness of the bar, while the flexural rigidity can be evaluated by inverting Eq.4 according to the following relationship:

$$E_f J = F \frac{L^3}{48\delta} \tag{5}$$

It can be noted that the vertical translational stiffness $\frac{48E_fJ}{L^3}$ corresponds to the slope of the force vs displacement relationship (Fig. 4b).

It is assumed that: (i) within the linear-elastic range of behaviour the flexural elastic modulus E_f remains constant along the entire bar length ($\overline{E_f}$) and (ii) the vertical load F and mid-span displacement δ are known from experiments (hence hereafter they will be referred to as F_{exp} and δ_{exp}, respectively). From these assumptions, it is then possible to introduce different approaches (see Fig. 5), of increasing complexity, to estimate the flexural elastic modulus $\overline{E_f}$ that matches the experimental

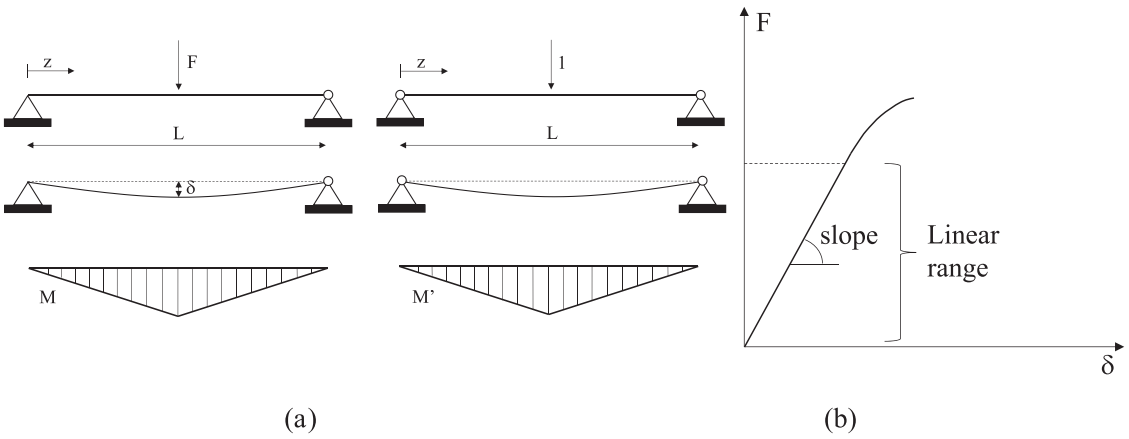

Fig. 4. (a) Static schematizations of the real and virtual systems for the evaluation of the mid-span displacement according to the principle of virtual works. (b) Qualitative representation of the force vs displacement response.

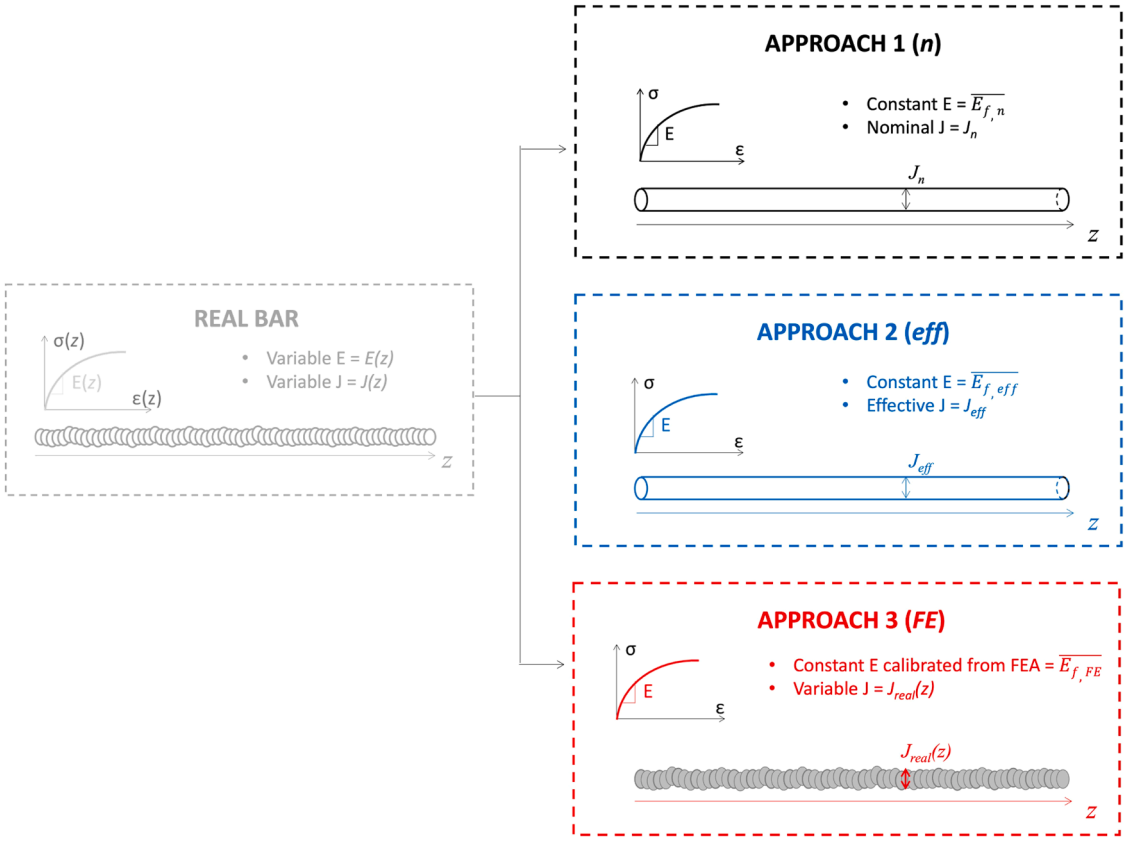

Fig. 5. Modelling approaches for WAAM bars.

flexural rigidity $(E_f J)_{\exp}$, as obtained from the slope of the experimental force vs displacement curve (Fig. 4b) according to Eq. 5.

- *Approach 1*: a nominal cylindrical bar is used to model the bar geometry. The geometrical model consists in a uniform cylinder with nominal geometry (d_n and J_n). The nominal flexural Young's modulus ($\overline{E_{f,n}}$) is evaluated through the following formulation:

$$\overline{E_{f,n}} = \frac{(E_f J)_{\exp}}{J_n} \tag{6}$$

- *Approach 2*: the effective cylindrical bar is used for the geometry. The geometrical model consists in a uniform cylinder with effective geometry (d_{eff} and J_{eff}). The effective flexural stiffness ($\overline{E_{f,eff}}$) is evaluated through the following formulation:

$$\overline{E_{f,eff}} = \frac{(E_f J)_{\exp}}{J_{eff}} \tag{7}$$

- *Approach 3*: the real geometry of the bar is used for the geometry. In this case, theoretically, the $\overline{E_f}$ could be estimated according to the following formulation:

$$\overline{E_f} = \frac{(E_f J)_{\exp}}{\frac{1}{L}\int_0^L J_{real}(z)dz} \tag{8}$$

In the FEA framework, the real geometry (J_{real}) is approximated by converting the 3D bar geometry obtained from high-precision laser scanning into a finite element model. Therefore, the constant flexural Young's modulus $\overline{E_f}$, can be calibrated through FEA . Hence, the calibrated flexural Young's modulus resulting from FEA is referred to as $\overline{E_{f,FE}}$.

It should be noted that the three approaches here introduced are mainly focused on the evaluation of the global influence of the main geometrical parameters and irregularities on the flexural elastic modulus of WAAM bars, which is assumed as a constant value along all the bar length. Thus, different advanced models should be considered to account for the possible non-uniform distribution of material elasticity along the single bar, which is, however, out of the scope of the present study.

Moreover, additional considerations on the limitations and degree of approximation of the proposed approaches are necessary. From the experimental investigations on the bending strength of WAAM bars, an integral-wise estimation of the flexural response (in terms of E_fJ) can be extracted. From that, the constant flexural elastic modulus $\overline{E_f}$ can be isolated from the geometrical part by following one of the 3 approaches introduced in the previous section. *Approach 1* is based on nominal geometrical quantities, hence it can be considered the most straightforward approach for preliminary structural design considerations. On the other hand, it completely disregards both sources of geometrical irregularities (e.g. the global specimen-to-specimen variability and the local inherent variability) associated with the repeatability and accuracy of the WAAM process. Therefore, the expected variability of the elastic modulus estimated according to *Approach 1* will include the two sources of geometric variability. *Approach 2* is based on volume-equivalent geometrical quantities, hence it requires a preliminary global geometrical characterization of the batch by means of volumetric measurements (as discussed in Section 3.2) to account for the global specimen-to-specimen variability in terms of effective geometrical parameters (d_{eff}, A_{eff}, J_{eff}). Therefore the expected variability of the elastic modulus estimated according to *Approach 2* will include the inherent local geometrical variability only. *Approach 3* is based on detailed information on the inherent geometrical irregularities of the printed part, hence it requires a detailed reconstruction of the actual geometry of the single bar, together with the development of advanced FEA (as discussed in Section 4). Therefore, the expected variability of the elastic modulus estimated according to *Approach 3* will include the additional sources of variability not directly related to the geometrical irregularities.

The aim of the present study is to estimate the flexural elastic modulus of WAAM bars from experimental tests following the three approaches as described before and compare their values and variabilities. The results will provide the reader with useful information on the level of approximation of each approach and will guide structural designers in the application of this new technology in the construction field.

3. Experimental methods

3.1. Material, process and samples production

A total of 10 bars of nominal length of 250 mm and nominal diameter of 6 mm were tested. The bars were fabricated by MX3D [31] adopting the dot-by-dot printing strategy. The bars tested under bending were then tested under compression to investigate their buckling behavior. All bars were manufactured with a fixed build angle of 0° and using the same set of process parameters. In detail, the welding source used was Gas Metal Arc Welding (GMAW) with the following process parameters: current of 100–140 A, arc voltage of 18–21 V, welding speed of 15–30 mm/s, wire feed rate of 4–8 m/min and deposition rate of 0.5–2 kg/h. It should be noted that the values of the process parameters provided are reported with their typical ranges as given by the manufacturer, while for more specific information the interested reader could refer directly to the manufacturer [31]. The average layer height was set to 1 mm. A commercially available standard stainless steel welding wire grade ER308LSi (1 mm diameter) supplied by Oerlikon [39] was used. The used substrate was made by a printing plate of 1000 × 1000×30 mm, with H-type beams welded as support.

3.2. Geometrical characterization

The geometrical characterization was performed at two different levels: (i) global characterization to quantify the effective geometrical parameters (at the batch level) and assess the specimen-to-specimen variability, (ii) local characterization to quantify the real geometry of each single bar and assess the inherent geometrical variability.

First, the specimen-to-specimen geometrical variability was assessed considering all specimens then tested under three-point bending. For each of them, the volume-equivalent, or effective, cross-sectional diameter (d_{eff}) and moment of inertia (J_{eff}) were estimated through hydraulic weights according to the Archimedes' principle to derive the volume-equivalent values. The procedure is detailed as follows: the weight on air (m_{air}) is taken from a digital scale while the weight inside water (m_{H20}) from an analogic hydraulic scale. Based on the two measures taken on the weight, the specimens' volume was derived from the calculated values of material density γ_v and density of water (at 25 °C) γ_{H20} with the following formulation: $V = (m_{air} - m_{H2O})/\gamma_{H2O}$. From the volume of each specimen, by assuming a cylindrical shape at first approximation, the effective diameter of the specimen (d_{eff}) was computed. The same procedure was utilized to evaluate the effective properties from tensile tests [40,41].

Then, the local geometrical measurements were performed through high precision 3D scanning technique considering the actual geometry of all the WAAM bars. First, the bars were 3D scanned with a structured-light projection Artec Spider 3D scanner [42]. The 3D model of the scanned bar consisted of around 40 million triangular elements, with a medium-points spacing of about 0.10 mm. From each 3D model, a total of 120 cross-sections (equally spaced at 2 mm) along the length of each specimen were extracted, from which detailed information regarding the local cross-sectional diameter d_{real} and moment of inertia J_{real} was derived. In particular, given the irregular shape of the real cross-section, the local cross-sectional diameter was estimated as the mean value of the two dimensions of the circumscribed rectangle, as described more in detail in [33]. From the value of d_{real}, the corresponding moment of inertia was computed assuming an equivalent circular shape, given the small deviations of the actual cross-sections from the circular shape.

It is worth noticing that the 2-mm spacing was selected as the result of a sensitivity analysis aimed at balancing the computational effort with the required level of accuracy in the reconstruction of the inertia variability along the length of the bar. The results of the sensitivity analysis are represented in Fig. 6 which compares, for a 100-mm central portion of the dot-2 bar, the along-the-length variability of the moment of inertia as obtained considering a 1-mm spacing and a 2-mm spacing, respectively. Given the purpose of the study to estimate the flexural rigidity of the bar, the results show that the two trends can be considered equivalent since: (i) their mean value is almost the same and (ii) they sufficiently well reproduce the surface oscillations induced by the manufacturing process. In fact, in this regard, it is important to highlight that the flexural rigidity is primarily influenced by the average moment of inertia rather than by its local oscillations around the mean value, since it is the result of an integral quantity (Eq. 8).

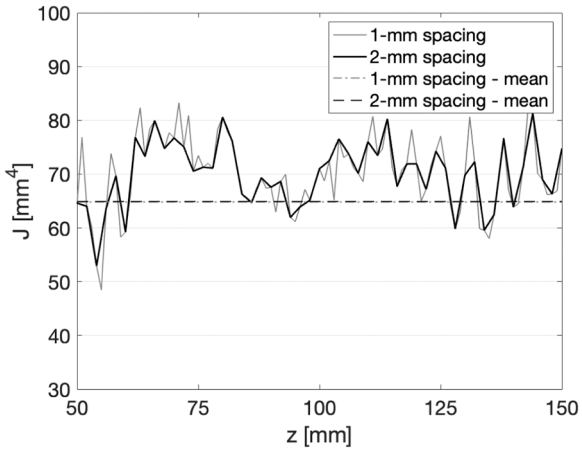

Fig. 6. Comparison between the moment of inertia variability along the length of the bar related to the 1-mm and 2-mm spacing acquisition from the 3D scanned geometry.

3.3. Mechanical characterization

Three-point bending tests were carried out on the 10 specimens of 250 mm length to evaluate their elastic flexural stiffness. The test set-up consisted of two fixed cylindrical supports spaced at 200 mm to mimick cylindrical hinge supports. The concentrated load was applied at the mid-span of the bar through an actuator in displacement control with a velocity of 2 mm/min, until the target displacement was reached. The target displacement was set at 2 mm, leading to a response that remained, overall, within the elastic limit. The value of the target displacement was evaluated by assuming isotropic material behavior and a Young's modulus value equal to E_t= 136.68 GPa based on the results of the previous tensile tests, see e.g. [26]. Under this assumption, the bending stress of the outermost fiber corresponding to a mid-span vertical displacement of 2 mm would result approximately equal to 200 MPa, thus lower than the expected value of the yielding stress (corresponding to the 0.2% proof stress, approximately equal to 250 MPa for bars printed at 0° build angle, see e.g. [26]). All tests were carried out according to ISO 178 specifications [43] at the LASTM lab of the University of Bologna using a 100 kN Amsler Wolpert testing machine with switch cabinet (Fig. 7). From each test the experimental value of the elastic flexural rigidity $(E_fJ)_{exp}$ was computed. First, the pseudo-plateau region was identified (corresponding to the linear branch of the force vs displacement response), then the flexural rigidity was determined by applying the Ordinary Least Square Regression (see Section 5.2).

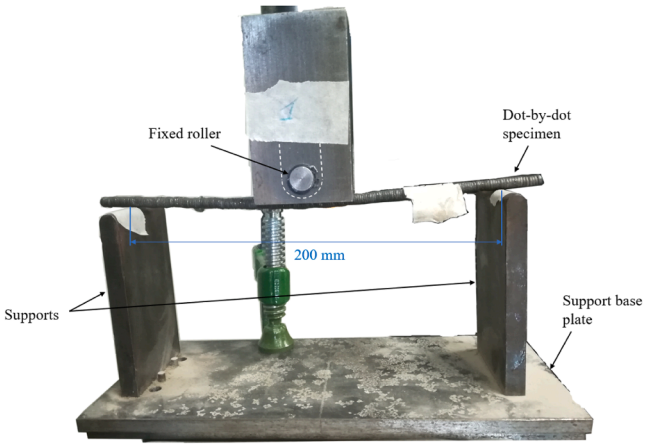

Fig. 7. Three-point bending test set-up.

4. Finite element analysis

4.1. The finite element models

FE analyses were carried out to estimate the flexural elastic modulus following the *Approach 3* introduced in Section 2.2. The FE models were based on the real geometrical information obtained through 3D scan acquisition to simulate the real geometrical irregularities of the printed bars and assess their influence on the flexural behavior. For the simulations, the computer-aided engineering (CAE) software Abaqus [44] was used. The 3D-scanned geometry was meshed with 10-node quadratic tetrahedral finite elements (C3D10).

The generation of the numerical models followed a two-step strategy. First, the complex 3D geometry of the part was reconstructed by lowering the resolution of the full 3D scan model to a given target percentage. Then the mesh of the FE model was created by considering tetrahedral finite elements of a constant nominal size. A mesh sensitivity analysis was carried out to select the proper mesh size aimed at balancing the computational effort and the accuracy in terms of global force-displacement response. Three different FE modelling strategies were considered. M1-type has a 2% 3D scan resolution and nominal mesh size of 0.5 mm, therefore it is considered as high-resolution geometrical model. M2-type has a 1% 3D scan resolution and a nominal mesh size of 0.75 mm, therefore it is considered as medium-resolution geometrical model. M3-type has a 0.5% 3D scan resolution and a nominal mesh size of 1.00 mm, therefore it is considered as low-resolution geometrical model. The M2-type modelling strategy was then chosen considering the results of the mesh sensitivity analysis, summarized in terms of the relative error in the estimation of the flexural rigidity R, as computed applying the Ordinary Least Square Regression (OLSR) within the linear branch of the global force vs mid-span displacement response. For illustrative purposes, the relative errors obtained for one specific bar (dot-2) are illustrated here. The relative error between M2 and M1 ($|R_{M2}- R_{M1}| / R_{M1}$) is equal to 1.57%, while the one between M3 and M2 ($|R_{M3}- R_{M2}| / R_{M2}$) is equal to 1.61%. Both relative errors are below the usual level of accuracy accepted in structural engineering. Similar results were obtained for the other specimens. They are not reported here for the sake of conciseness.

The Ramberg-Osgood (RO) [45] material model was adopted for the constitutive model of WAAM stainless steel resulting from the dot-by-dot deposition process, considering the following initial values of the main parameters calibrated from the tensile tests on WAAM bars: elastic modulus E_0= E_t= 137 GPa,exponent $n = 8.59$, 0.01% proof stress (representative of the proportionality limit) $\sigma_{0.01}$= 180 MPa and 0.2% proof stress (representative of yielding stress) $\sigma_{0.2}$= 250 MPa (see e.g. [26]). From the engineering stress-strain curve adopted following the RO material model, the true stress-strain curve was calculated and adopted in the FEA. In detail, an elastic-plastic behavior was modelled in Abaqus software. The stress at the elastic limit has been set equal to $\sigma_{0.01}$. For the plastic true stress-strain curve, the following relationship was implemented [46]:

$$\varepsilon_{pl,true} = \varepsilon_{true} - \frac{\sigma_{true}}{E} \tag{9}$$

Where:

$$\varepsilon_{true} = \ln\left(1 + \varepsilon_{eng}\right) \tag{10}$$

$$\sigma_{true} = \sigma_{eng}\left(1 + \varepsilon_{eng}\right) \tag{11}$$

Fig. 8 depicts the initial true stress-strain model (e.g. at the beginning of the iterative process described in Section 4.1), as computed from the mean engineering one (according to Eqs. 9–11).

For the application of boundary and loading conditions, three reference points (RP) were set in terms of fixed points defined by a set of coordinates. These points were used to fix the position of both boundary

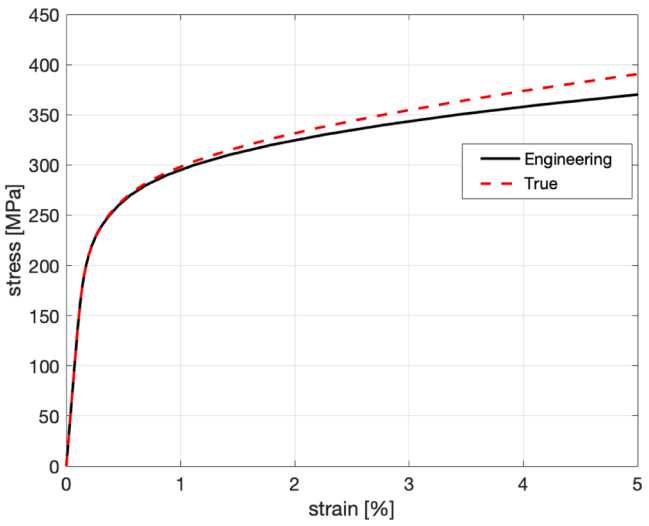

Fig. 8. Initial engineering and true stress-strain curves adopted for the FEA.

conditions and loading point for all the models. In detail, two reference points (RP-1 and RP-2) were set at a relative distance equal to 200 mm to simulate the position of the physical hinge-supports of the experimental set-up. The third reference point (RP-3) was set at the mid-span where the load is applied. The boundary conditions were set as follows. A hinge (i.e. null displacements u_x=u_y=u_z=0 and null out-of-plane rotations φ_z=φ_y=0) was considered for RP-1, while a roller was considered for RP-2 (i.e. null displacements u_x=u_y=0 and null out-of-plane rotations φ_z=φ_y=0). The out-of-plane displacement (u_x=0) and rotations (φ_z=φ_y=0) were constrained for RP3. The constraints were imposed by tying the cross-sections corresponding to the support sections and loading point at mid-span with the respective reference points. The increasing load at the midspan was applied by monitoring the vertical displacement of RP-3. The analysis was carried out as non-linear static in displacement control of the midspan with an increment of 0.01 mm per step. Fig. 9 provides the graphical representation of one dot-by-dot WAAM bar together with the reconstructed geometry from high-precision 3D scanning and the mesh of FE model with an indication of the reference points and constraints.

4.2. The calibration of the flexural Young's modulus

The calibration of the flexural Young's modulus $\overline{E_{f,FE}}$ was performed through an iterative procedure considering the 3D-scanned geometry of all specimens. A non-linear incremental static analysis was carried out by applying an increasing vertical displacement at the mid-span reference point up to the 2 mm target displacement value. The numerical force-displacement curves from FEA were compared with the ones obtained from the experimental tests (see Section 5). In detail, the two curves were compared in terms of rigidity (*EJ*) values taken within the linear-elastic region of the curve and applying the Ordinary Least Square Regression (OLSR). From the obtained rigidity (*EJ*) values, the calibrated flexural elastic modulus $\overline{E_{f,FE}}$ was computed according to Eq. 8 using the corresponding average moment of inertia J_{real} (whose values are provided in Section 5.1, Table 2). The calibrated value of $\overline{E_{f,FE}}$ was then introduced in the FEA model until the relative error between the two values of flexural rigidity (i.e. $(E_fJ)_{FE}$ and $(E_fJ)_{\exp}$) was negligible (below 1%).

5. Main results and discussion

5.1. Results of the geometrical characterization

In order to evaluate the effective mechanical properties for structural design purposes, a volume-equivalent uniform circular cross-section of diameter d_{eff} was assumed to obtain the corresponding effective cross-sectional moment of inertia $J_{eff} = \frac{\pi d_{eff}^4}{64}$. The values of the effective diameters and moments of inertia for all tested specimens are reported in Table 1. The average effective diameter d_{eff} results equal to 6.01 mm, therefore practically equal to the nominal diameter from the digital input (6 mm) with a very small coefficient of variation equal to 0.5%. The corresponding average effective moment of inertia J_{eff} results equal to 64.13 mm^4 with 1.8% coefficient of variation. This result indicates that the investigated WAAM process has an overall good repeatability.

In addition, the inherent cross-sectional variability was investigated by considering the 3D scanned models of all tested specimens. For each specimen, the distribution of the local cross-sectional diameters d_{real} and moment of inertia J_{real} was evaluated according to the procedure detailed in Section 3.2. For each specimen, the mean and COV values of J_{real} and d_{real} are reported in Table 2 together with the mean and COV values across the whole batch. The across-the-batch mean value of d_{real} is equal to 5.97 mm, therefore practically coincident with the nominal one (6 mm). The COV values for the single specimens are, on average, equal

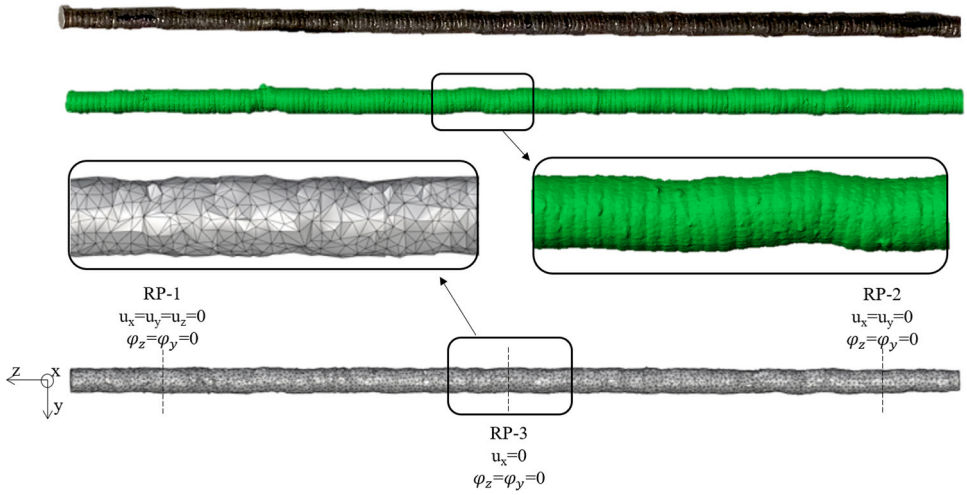

Fig. 9. Graphical comparison between the real bar (top), the geometry obtained from the high-precision 3D scanning (mid) and the FE model with indication of the reference points and constraints (bottom).

Table 1
Effective cross-sectional diameters and moments of inertia for the tested bars: specimen-to-specimen variability (from volume measures).

Specimen-to-specimen variability		
Specimen ID	J_{eff} [mm^4]	d_{eff} [mm]
dot-1	64.90	6.03
dot-2	64.04	6.01
dot-3	63.62	6.00
dot-4	64.04	6.01
dot-5	63.19	5.99
dot-6	64.90	6.03
dot-7	62.77	5.98
dot-8	64.47	6.02
dot-9	66.64	6.07
dot-10	62.77	5.98
Mean (batch)	**64.13**	**6.01**
COV (batch)	**1.8%**	**0.5%**

Table 2
Mean values and standard deviations of real cross-sectional diameters and moments of inertia for the tested bars: inherent variability (from 3D scan measures).

Inherent variability				
Specimen ID	J_{real}		d_{real}	
	Mean (single) [mm^4]	COV (single) [%]	Mean (single) [mm]	COV (single) [%]
dot-1	59.44	15%	5.88	4%
dot-2	64.90	17%	6.01	5%
dot-3	63.24	14%	5.98	4%
dot-4	62.01	14%	5.95	4%
dot-5	62.72	18%	5.96	5%
dot-6	66.28	24%	6.03	6%
dot-7	60.49	21%	5.90	6%
dot-8	63.10	19%	5.97	5%
dot-9	64.38	16%	6.00	4%
dot-10	63.27	16%	5.98	4%
Mean (batch)	**62.98**	**17%**	**5.97**	**5%**
COV (batch)	**3.2%**	/	**0.7%**	/

to 17% (for J_{real}) and 5% (for d_{real}), while the across-the-batch COV is equal to roughly 3% for J_{real} and 0.7% for d_{real}. It can be noted that the single specimen COV of J_{real} is in line with results obtained from previous 3D scanned models of similar bars (see e.g. [26]) manufactured by the same producer. This observation indicates that the investigated WAAM process has a sufficient global repeatability at the scale of different production batches.

More in detail, by comparing the values of the single specimen and across-the-batch COV it clearly appears that the local inherent geometrical variability is significantly higher than the global specimen-to-specimen variability (i.e., at the entire batch level). Note that the latter COV values are in good agreement with the COV values based on volume measurements as reported in Table 1. This indicates that the two measurement strategies lead to similar results when used for the assessment of the effective geometrical parameters.

Fig. 10 compares the volume-based and 3D-scan measurements of the cross-sectional moments of inertia and diameters for all specimens. It should be noted that the grey areas indicate the two end-portions of the bars (25-mm length) that extend out of the two supports of the three-point bending test set-up (see Fig. 7). It is worth noticing that all the specimens are characterized by a first portion with a reduced diameter and moment of inertia. This could be due to the different sets of temperature between the base plate and the printed bars, which affect the first layers of printing. On average, the 3D scan-based (black dashed line) and volume-based (red dashed line) measurements are in quite close agreement with each other, with an average relative error of around 0.9%.

5.2. Results of the three-point bending test

The global results of three-point bending tests in terms of applied force F_{exp} vs mid-span deflection δ_{exp} are shown in Fig. 11a. As expected, all the specimens tested up to a target displacement of 2 mm experienced a similar almost-linear elastic behavior. For each value of imposed vertical displacement, the experimental flexural rigidity $(E_fJ)_{exp}$ was calculated according to Eq. 5. For illustrative purposes, Fig. 11b provides the graph of $(E_fJ)_{exp}$ vs δ_{exp} for a specific test (dot-3). Once the pseudo-plateau region was visually identified (red dotted portion of the graph), Ordinary Least Square Regression was used to fit the branch.

Table 3 presents the computed values of the experimental flexural rigidity $(E_fJ)_{exp}$. The COV value is equal to 6%. It is of interest to notice that the value is almost twice the COV value obtained for the effective moment of inertia (as reported in Table 1) and for the average real moment of inertia (as reported in Table 2). The comparison suggests that the large variability of the flexural rigidity cannot be uniquely attributed to the specimen-to-specimen variability of the moment of inertia.

5.3. Results of the Finite Element Analysis

The Finite Element Analysis (FEA) was carried out considering the 3D-scanned geometry of all specimens to create a close-to-real imperfect geometry of the printed bars. The aim is to calibrate the values of flexural elastic modulus $\overline{E_{f,FE}}$ following *Approach 3* (as introduced in Section 2) and the procedure explained in Section 4.2. At the beginning of the iterative process, the initial value of $\overline{E_{f,FE}}$ was set equal to E_t.

Fig. 12 displays the deformed shape and the bending stress contour (σ_{11}) of dot-1 specimen as obtained at the last step of the simulated three-point bending test corresponding to a mid-point vertical displacement of 2 mm. It can be noticed that the peak stresses are around 250 MPa, thus confirming that the specimen remained within the elastic field during the whole test.

The calibration procedure described in Section 4.2 was applied to all tested specimens. Table 4 collects the results in terms of flexural elastic moduli $\overline{E_{f,FE}}$ from FEA. On average, the $\overline{E_{f,FE}}$ value results equal to 113 GPa with a COV value equal to 8%, thus close to the COV exhibited by the experimental flexural rigidity. It can be noticed that the average flexural elastic modulus obtained from FEA is much lower than the standard value of Young's modulus of conventionally manufactured stainless steel for structural applications, in the range of 195–200 GPa [47]. Additional considerations are given in the next section.

5.4. Discussion on the results

The results obtained comparing the three proposed approaches for the evaluation of the flexural modulus of inertia allow us to make some useful considerations for structural design purposes. For this aim, Tables 5 and 6 provide a comprehensive overview of the main results from the geometrical and mechanical characterization. They are useful to assess the accuracy of the proposed methods and compare the influence of the different sources of uncertainties in the estimation of the flexural elastic moduli.

Table 5 compares the values of the nominal J_n, effective J_{eff} (from volume measurements) and average $J_{real,m}$ (from 3D scanning) moments of inertia. As already noticed in Section 5.1, the values of the effective and average moments of inertia are in good mutual agreement, thus indicating the good reliability of the two measurement methods. The ratios J_{eff}/J_n, $J_{real,m}/J_n$ and $J_{real,m}/J_{eff}$ are centered to values which are very close to 1.0 (0.98–1.01), while their maximum/minimum values are within the range of 1.05–0.95 indicating that the maximum relative errors are less than or equal to 5%. Moreover, the low COV values (2–3%) confirm that the investigated WAAM process has a good overall (at the level of the entire batch) repeatability.

Table 6 compares the values of the nominal, effective and FE-based

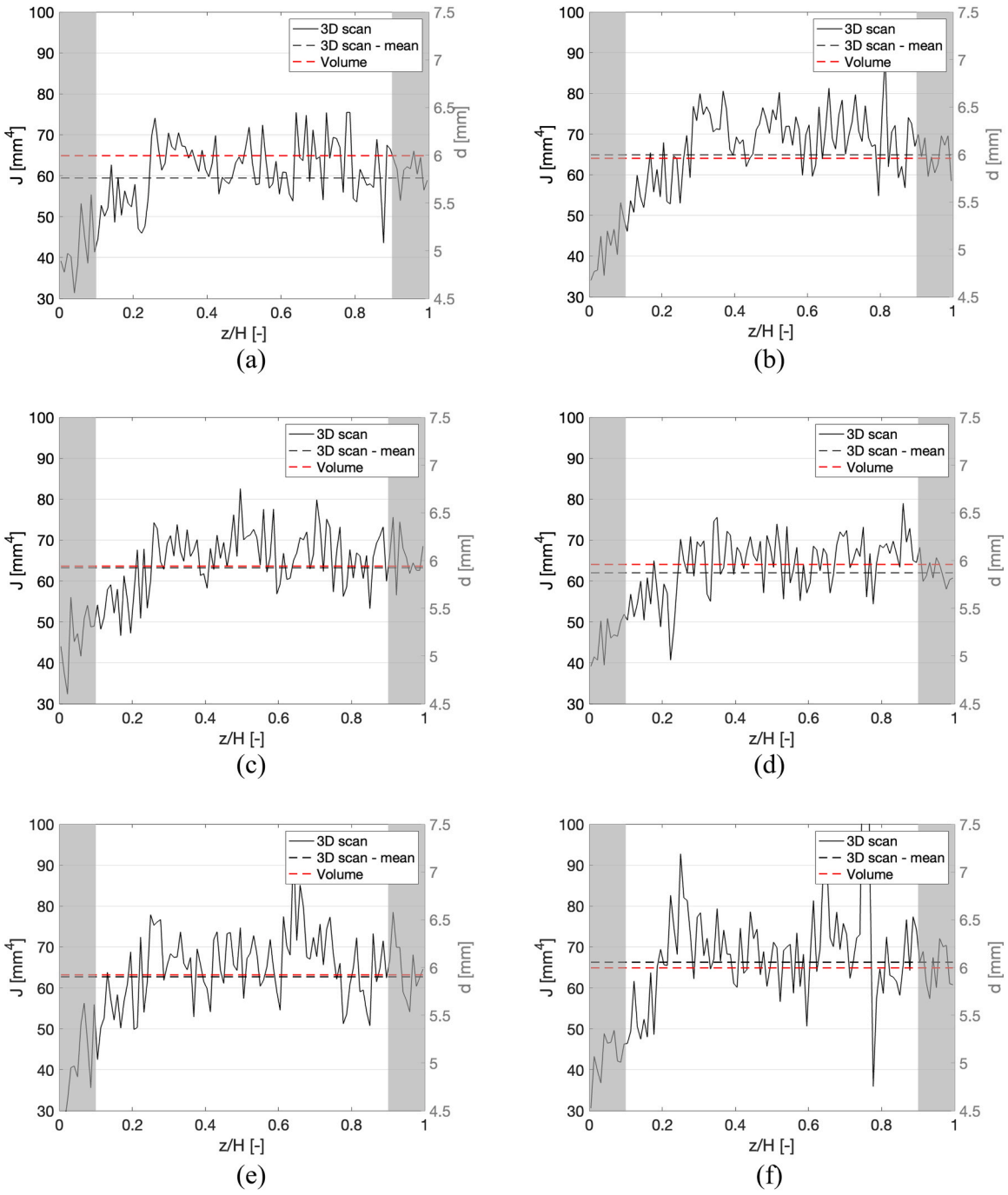

Fig. 10. Comparison between along-the-length bar diameter and moment of inertia as obtained from 3D scan and effective values from volume measures: (a) dot-1 specimen; (b) dot-2 specimen; (c) dot-3 specimen; (d) dot-4 specimen; (e) dot-5 specimen; (f) dot-6 specimen; (g) dot-7 specimen; (h) dot-8 specimen; (i) dot-9 specimen; (j) dot-10 specimen.

flexural elastic moduli evaluated following the three approaches introduced in Section 2.2.

The three mean values of $\overline{E_{f,n}}$, $\overline{E_{f,eff}}$ and $\overline{E_{f,FE}}$ are practically identical (113–114 GPa) to each other. The three ratios $\frac{\overline{E_{f,eff}}}{\overline{E_{f,n}}}$, $\frac{\overline{E_{f,FE}}}{\overline{E_{f,n}}}$ and $\frac{\overline{E_{f,FE}}}{\overline{E_{f,eff}}}$ are, on average, centered to 1.0 while their maximum/minimum values are equal to 1.16 and 0.86. These findings indicate that none of the three methods leads to a biased estimation and that their relative discrepancies are within ±15%. It is also of interest to notice that the mean value of the flexural elastic modulus corresponds, on average, to around 86% of the effective tensile elastic modulus (E_t) as evaluated through tensile tests on vertically printed bars (dot-0) manufactured with the same set of process parameters, see e.g. [26], which resulted equal to 137 GPa. This finding indicates that the anisotropic behavior of dot-by-dot WAAM bar is also affected by the type of internal force, apart from the process parameters and build angle, the latter being previously investigated in [26] in relation to the behavior under tensile axial forces.

The three COV values are close to each other with values between 6–8%, significantly higher than the COV exhibited by the moment of inertia. The result indicates that neither the use of the effective geometry nor the use of the real geometry leads to an appreciable reduction of the dispersion in the estimation of the flexural rigidity. These findings

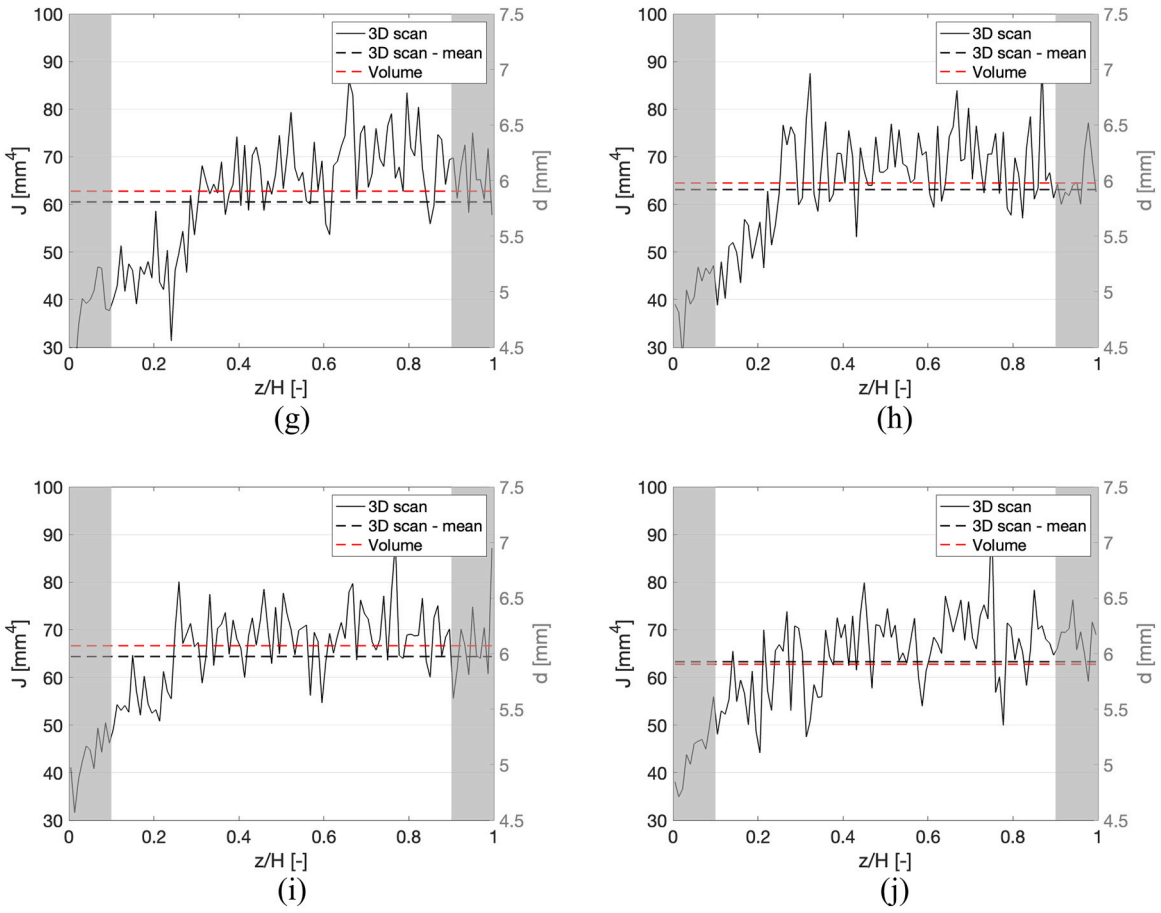

Fig. 10. (*continued*).

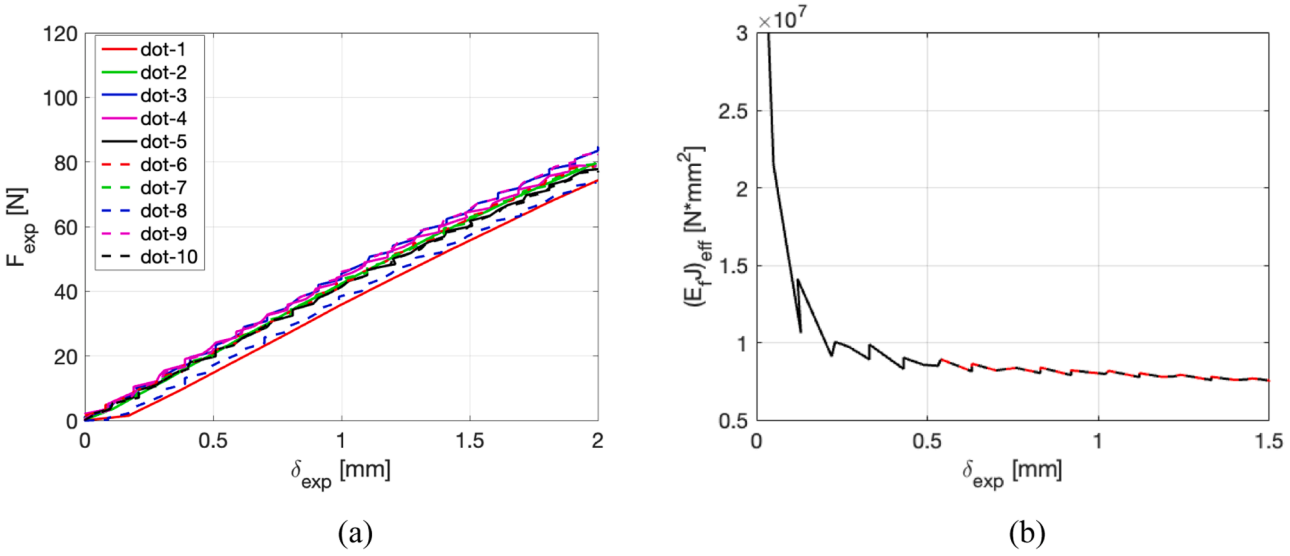

Fig. 11. (a) Force vs. displacement curves from three-point bending tests; (b) Flexural stiffness vs. mid-span displacement for dot-3 specimen.

Table 3
Flexural rigidity from three-point bending tests.

Spec ID	dot-1	dot-2	dot-3	dot-4	dot-5	dot-6	dot-7	dot-8	dot-9	dot-10	Mean	COV
$(E_fJ)_{exp}$ [10^6N•m^2]	6.37	7.39	7.75	7.51	7.27	7.27	7.39	6.64	7.85	7.25	**7.37**	**6%**

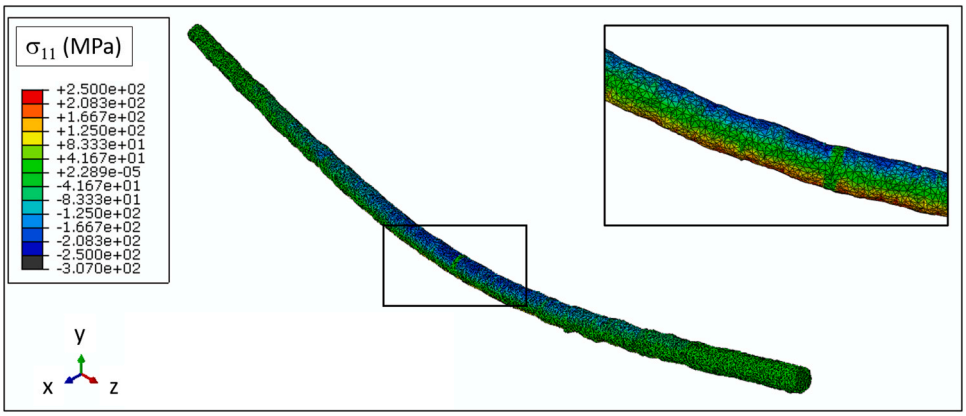

Fig. 12. Deformed shape (magnified) and bending stress contour map for dot-1 specimen at the last step of the simulation.

Table 4
Flexural elastic modulus from FEA.

Spec ID	dot-1	dot-2	dot-3	dot-4	dot-5	dot-6	dot-7	dot-8	dot-9	dot-10	Mean	COV
$\overline{E_{f,FE}}$ **[GPa]**	113.80	102.64	119.58	124.19	113.50	107.05	124.44	102.14	105.63	121.46	**113.44**	**8%**

Table 5
Overview of the results in terms of cross section moment of inertia.

Specimen ID	J_n [mm^4]	J_{eff} [mm^4]	$J_{real,m}$ [mm^4]	J_{eff}/J_n [-]	$J_{real,m}/J_n$ [-]	$J_{real,m}/J_{eff}$ [-]
dot-1	63.62	64.90	59.44	1.02	0.93	0.92
dot-2	63.62	64.04	64.90	1.01	1.02	1.01
dot-3	63.62	63.62	63.24	1.00	0.99	0.99
dot-4	63.62	64.04	62.01	1.01	0.97	0.97
dot-5	63.62	63.19	62.72	0.99	0.99	0.99
dot-6	63.62	64.90	66.28	1.02	1.04	1.02
dot-7	63.62	62.77	60.49	0.99	0.95	0.96
dot-8	63.62	64.47	63.10	1.01	0.99	0.98
dot-9	63.62	66.64	64.38	1.05	1.01	0.97
dot-10	63.62	62.77	63.27	0.99	0.99	1.01
Mean	**63.62**	**64.13**	**62.98**	**1.01**	**0.99**	**0.98**
COV	/	**2%**	**3%**	**2%**	**3%**	**3%**

Table 6
Overview of the results of flexural elastic moduli based on the 3 approaches.

Specimen ID	$\overline{E_{f,n}}$ [GPa]	$\overline{E_{f,eff}}$ [GPa]	$\overline{E_{f,FE}}$ [GPa]	$\frac{\overline{E_{f,eff}}}{\overline{E_{f,n}}}$ [-]	$\frac{\overline{E_{f,FE}}}{\overline{E_{f,n}}}$ [-]	$\frac{\overline{E_{f,FE}}}{\overline{E_{f,eff}}}$ [-]
dot-1	100.13	98.13	113.80	0.98	1.14	1.16
dot-2	116.16	115.39	102.64	0.99	0.88	0.89
dot-3	121.82	121.77	119.58	1.00	0.98	0.98
dot-4	118.05	116.54	124.19	0.99	1.05	1.07
dot-5	114.28	115.05	113.50	1.01	0.99	0.99
dot-6	114.28	112.02	107.05	0.98	0.94	0.96
dot-7	116.16	117.77	124.44	1.01	1.07	1.06
dot-8	104.37	102.92	102.14	0.99	0.98	0.99
dot-9	123.39	117.75	105.63	0.95	0.86	0.90
dot-10	113.96	114.65	121.46	1.01	1.07	1.06
Mean	**114.26**	**113.20**	**113.44**	**0.99**	**1.00**	**1.00**
COV	**6%**	**6%**	**8%**	**2%**	**9%**	**8%**

suggest that the investigated WAAM process probably induces some non-negligible intrinsic variability on the flexural elastic modulus that is not correlated to the geometrical variability. In fact, this additional source of variability seems not to be reduced when considering the real geometrical variability of the printed element according to the proposed *Approach 3*.

In light of the obtained results, it can be noted that the three proposed approaches, despite the increasing levels of accuracy in the geometrical description of the bar (from nominal to the effective values, up to a close-to-real description based on an accurate 3D scan), provide a similar estimation of the flexural elastic modulus, also in terms of specimen-to-specimen variability. Therefore, based on the obtained results (whose quantitative values are valid only for the investigated WAAM process), the use of nominal geometry for the evaluation of the global flexural stiffness can be considered a reasonable choice for the investigated WAAM process when dealing with structural design purposes. However, additional investigations aimed at correlating the printing parameters with the microstructure and key mechanical parameters are necessary to confirm this interpretation and, possibly, extend the recommendations for other sets of process parameters.

6. Conclusions

The present study aims at assessing the elastic flexural behaviour of dot-by-dot Wire-and-Arc Additively Manufactured (WAAM) stainless steel bars through experimental characterization combined with analytical evaluations and FEA. The main novelty of the work lies in the assessment of the flexural elastic modulus, considering a specific set of process parameters and a single build angle, and its variability with respect to the inherent geometrical irregularities induced by the manufacturing process.

The geometrical and mechanical characterizations were carried out to assess the flexural stiffness of WAAM bars following three approaches of increasing complexity, based on different considerations related to the geometrical irregularities at both the global (entire batch) and local level (single specimen). At first, detailed investigations on the geometrical characterization through volume measures and 3D scan acquisition were performed. Three-points bending tests were carried out to obtain the experimental values of the elastic flexural stiffness from the slope of the experimental vertical force vs mid-span displacement response. From the experimental flexural stiffness, the flexural Young's modulus was calibrated according to the three introduced approaches, the first two leading to simplified analytical formulations (based on the nominal and effective geometry of an equivalent uniform cylindrical specimen), while the third requiring more advanced numerical simulations through FEA and the accurate reconstruction of the real geometry of the bar as obtained from high-precision 3D-scanning. The comparisons between the values of the flexural elastic modulus obtained according to the three approaches allow us to evaluate, in an average sense, the effect of the

geometrical irregularities.

The main results from the geometrical characterization allow us to draw the following conclusions. The effective values (evaluated from volume equivalency) and mean values across the batch (evaluated from 3D scanning) of both diameter and moment of inertia are, on average, almost coincident with the nominal values. Moreover, they exhibit very reduced variability with COV values of about 0.5%− 0.7% for the diameters and 2–3% for the moments of inertia. The low COV indicates an overall good repeatability of the investigated dot-by-dot printing process. The results of the investigations in terms of inherent cross-sectional variability at the level of the single specimen indicate that the specific dot-by-dot WAAM process has a limited precision since the COV values for the diameter and moment of inertia are of about 4% and 15%, respectively.

The results of the three-point bending tests and FEA allow us to draw the following conclusions. The flexural elastic modulus as evaluated according to the three proposed approaches is approximately equal, on average, to 113 GPa. In fact, in an average sense, the nominal $\overline{E_{f,n}}$ (e.g. taken considering the nominal moment of inertia), the effective $\overline{E_{f,eff}}$ (e.g. based on effective volume based geometrical measurements) and the $\overline{E_{f,FE}}$ (e.g. based on FEA) closely match. However, it differs substantially from the average tensile elastic modulus exhibited by similar vertically printed bars manufactured with the same set of process parameters, whose average value was equal to 137 GPa. This discrepancy indicates that the anisotropic response is also affected by the type of internal force. Moreover, the maximum relative differences between the flexural elastic moduli evaluated according to the three methods are limited within a range of $\pm$ 15%. Regarding the variability of the results, the quite high and constant COV value (6–8%) of the flexural elastic modulus obtained from the three approaches indicates that the printing process may induce an additional source of variability in the elastic properties of the bars that cannot be uniquely attributed to the geometrical irregularities. Overall the results indicate that, for the investigated dot-by-dot WAAM technology, the use of nominal geometry for the evaluation of the flexural behavior can be considered a reasonable choice for design purposes.

However, additional investigations aimed at correlating the printing parameters with the microstructure and key mechanical parameters are necessary to confirm this possible interpretation.

As a further remark, it is necessary to highlight that the quantitative results should be applied only to bars having similar geometrical properties and fabricated with the same WAAM technology. In order to obtain trends of more general validity, a wider experimental investigation on bars of different geometrical properties (diameters and lengths) and produced with different WAAM technologies is necessary.

Finally, the obtained preliminary results could pave the way toward a more comprehensive interpretation of the buckling behavior of WAAM slender elements. The calibrated flexural elastic modulus could, in fact, be used to investigate the buckling behavior of WAAM bars under compression and then to calibrate ad-hoc buckling curves for structural design purposes.

CRediT authorship contribution statement

Laghi Vittoria: Writing – review & editing, Writing – original draft, Investigation, Conceptualization. **palermo michele:** Writing – review & editing, Writing – original draft, Conceptualization. **Trombetti Tomaso:** Supervision, Resources. **Gasparini Giada:** Writing – review & editing. **Girella Valentina Alena:** Investigation.

Declaration of Competing Interest

The authors declare that they have no known competing financial interests or personal relationships that could have appeared to influence the work reported in this paper.

Data availability

Data will be made available on request.

Acknowledgements

The support of Dutch company MX3D held in Amsterdam is gratefully acknowledged for giving the additive-manufactured elements tested.

Dr. Vittoria Laghi gratefully acknowledges the financial support of “Young Researchers” – Seal of Excellence 2022 grant - funded on D.M. 737/2021 resources-funded by European Union – “NextGenerationEU".

Dr. Laghi gratefully acknowledges the L′Oreal-UNESCO “For Women in Science” program for the financial support.

References

[1] Derekar KS. A review of wire arc additive manufacturing and advances in wire arc additive manufacturing of aluminium. Mater Sci Technol 2018;34:895–916. https://doi.org/10.1080/02670836.2018.1455012.
[2] Rodrigues TA, Duarte V, Miranda RM, Santos TG, Oliveira JP. Current status and perspectives on wire and arc additive manufacturing (WAAM). Materials 2019;12. https://doi.org/10.3390/ma12071121.
[3] Buchanan C, Gardner L. Metal 3D printing in construction: a review of methods, research, applications, opportunities and challenges. Eng Struct 2019;180:332–48. https://doi.org/10.1016/j.engstruct.2018.11.045.
[4] Kyvelou P, Slack H, Daskalaki Mountanou D, Wadee MA, Britton TBen, Buchanan C, et al. Mechanical and microstructural testing of wire and arc additively manufactured sheet material. Mater Des 2020;192:108675. https://doi.org/10.1016/j.matdes.2020.108675.
[5] Gordon JV, Haden CV, Nied HF, Vinci RP, Harlow DG. Fatigue crack growth anisotropy, texture and residual stress in austenitic steel made by wire and arc additive manufacturing. Mater Sci Eng A 2018;724:431–8. https://doi.org/10.1016/j.msea.2018.03.075.
[6] Laghi V, Palermo M, Gasparini G, Girelli VA, Trombetti T. On the influence of the geometrical irregularities in the mechanical response of wire-and-arc additively manufactured planar elements. J Constr Steel Res 2021;178:106490. https://doi.org/10.1016/j.jcsr.2020.106490.
[7] Gardner L, Kyvelou P, Herbert G, Buchanan C. Testing and initial verification of the world’s first metal 3D printed bridge. J Constr Steel Res 2020;172. https://doi.org/10.1016/j.jcsr.2020.106233.
[8] Wu B, Pan Z, Ding D, Cuiuri D, Li H, Xu J, et al. A review of the wire arc additive manufacturing of metals: properties, defects and quality improvement. J Manuf Process 2018. https://doi.org/10.1016/j.jmapro.2018.08.001.
[9] Treutler K, Wesling V. The current state of research of wire arc additive manufacturing (WAAM): a review. Appl Sci 2021;11:8619.
[10] Laghi V, Palermo M, Gasparini G, Trombetti T. Computational design and manufacturing of a half-scaled 3D-printed stainless steel diagrid column. Addit Manuf 2020;36. https://doi.org/10.1016/j.addma.2020.101505.
[11] Kloft H, Empelmann M, Hack N, Herrmann E, Lowke D. Reinforcement strategies for 3D-concrete-printing. Civ Eng Des 2020;2:131–9. https://doi.org/10.1002/cend.202000022.
[12] Mechtcherine V, Buswell R, Kloft H, Bos FP, Hack N, Wolfs R, et al. Integrating reinforcement in digital fabrication with concrete: a review and classification framework. Cem Concr Compos 2021;119:103964. https://doi.org/10.1016/j.cemconcomp.2021.103964.
[13] Evans SI, Wang J, Qin J, He Y, Shepherd P, Ding J. A review of WAAM for steel construction – manufacturing, material and geometric properties, design, and future directions. Structures 2022;44:1506–22. https://doi.org/10.1016/J.ISTRUC.2022.08.084.
[14] Gardner L. Metal additive manufacturing in structural engineering – review, advances, opportunities and outlook. Structures 2023;47:2178–93. https://doi.org/10.1016/J.ISTRUC.2022.12.039.
[15] Huang C, Kyvelou P, Gardner L. Stress-strain curves for wire arc additively manufactured steels. Eng Struct 2023;279:115628. https://doi.org/10.1016/J.ENGSTRUCT.2023.115628.
[16] Huang C, Meng X, Gardner L. Cross-sectional behaviour of wire arc additively manufactured tubular beams. Eng Struct 2022;272. https://doi.org/10.1016/J.ENGSTRUCT.2022.114922.
[17] Hadjipantelis N, Weber B, Gardner L. Characterisation of the anisotropic response of wire and arc additively manufactured stainless steel. Ce/Pap 2021;4:1757–66.
[18] L. Gardner, P. Kyvelou, C. Buchanan, Testing of wire and arc additively manufactured tubular sections, (2019) 978–981. https://doi.org/10.3850/978–981-11–0745-0.
[19] Kyvelou P, Huang C, Gardner L, Buchanan C. Structural testing and design of wire arc additively manufactured square hollow sections. J Struct Eng 2021;147:04021218. https://doi.org/10.1061/(ASCE)ST.1943-541X.0003188.
[20] Huang C, Meng X, Buchanan C, Gardner L. Flexural buckling of wire arc additively manufactured tubular columns. J Struct Eng 2022;148:04022139. https://doi.org/10.1061/(ASCE)ST.1943-541X.0003427.

[21] Zhang R, Gardner L, Buchanan C, Matilainen VP, Piili H, Salminen A. Testing and analysis of additively manufactured stainless steel CHS in compression. Thin Walled Struct 2021;159:107270. https://doi.org/10.1016/J.TWS.2020.107270.
[22] T. Feucht J. Lange 3-d-printing with steel: additive manufacturing of connection elements Adv Eng Mater, Struct Syst: Innov, Mech Appl - Proc 7th Int Conf Struct Eng, Mech Comput 2019 2019 419 424 doi: 10.1201/9780429426506-75.
[23] Lange J, Feucht T, Erven M. 3D printing with steel: additive manufacturing for connections and structures, Steel. Construction 2020;13:144–53.
[24] T. Feucht, B. Waldschmitt, J. Lange, M. Erven, Additive manufacturing of a bridge in situ Nominated for Eurosteel 2021 Best Paper Award, (2022). https://doi.org/10.1002/stco.202100045.
[25] Müller J, Grabowski M, Müller C, Hensel J, Unglaub J, Thiele K, et al. Design and parameter identification of wire and arc additively manufactured (WAAM) steel bars for use in construction. Metals 2019;9:725. https://doi.org/10.3390/met9070725.
[26] Laghi V, Palermo M, Tonelli L, Gasparini G, Girelli VA, Ceschini L, et al. Mechanical response of dot-by-dot wire-and-arc additively manufactured 304L stainless steel bars under tensile loading. Constr Build Mater 2022;318:125925.
[27] Silvestru V-A, Ariza I, Vienne J, Michel L, Aguilar Sanchez AM, Angst U, et al. Performance under tensile loading of point-by-point wire and arc additively manufactured steel bars for structural components. Mater Des 2021;205:109740. https://doi.org/10.1016/j.matdes.2021.109740.
[28] Silvestru VA, Ariza I, Taras A. Structural behaviour of point-by-point wire arc additively manufactured steel bars under compressive loading. J Constr Steel Res 2023;207:107982. https://doi.org/10.1016/J.JCSR.2023.107982.
[29] K. Tischner, S. Rappl, F. Riegger, A. Strasser, K. Osterminski, T. Kraenkel, et al. , Bond Behavior of WAAM Reinforcements in Comparison to Conventional Steel Reinforcements, (2023). https://doi.org/10.3390/constrmater3020014.
[30] Dörrie R, Laghi V, Arrè L, Kienbaum G, Babovic N, Hack N, et al. Combined additive manufacturing techniques for adaptive coastline protection structures. 2022, Vol. 12, Page 1806 Buildings 2022;12:1806. https://doi.org/10.3390/BUILDINGS12111806.
[31] MX3D Webpage, (n.d.). www.mx3d.com.
[32] Laghi V, Palermo M, Gasparini G, Veljkovic M, Trombetti T. Assessment of design mechanical parameters and partial safety factors for wire-and-arc additive manufactured stainless steel. Eng Struct 2020;225:111314. https://doi.org/10.1016/j.engstruct.2020.111314.
[33] Laghi V, Palermo M, Gasparini G, Girelli VA, Trombetti T. Experimental results for structural design of wire-and-arc additive manufactured stainless steel members. J Constr Steel Res 2020;167. https://doi.org/10.1016/j.jcsr.2019.105858.
[34] Laghi V, Tonelli L, Palermo M, Bruggi M, Sola R, Ceschini L, et al. Experimentally-validated orthotropic elastic model for wire-and-arc additively manufactured stainless steel. Addit Manuf 2021;42:101999. https://doi.org/10.1016/j.addma.2021.101999.
[35] Hadjipantelis N, Weber B, Buchanan C, Gardner L. Description of anisotropic material response of wire and arc additively manufactured thin-walled stainless steel elements. Thin Walled Struct 2022;171:108634. https://doi.org/10.1016/J.TWS.2021.108634.
[36] Laghi V, Palermo M, Tonelli L, Gasparini G, Ceschini L, Trombetti T. Tensile properties and microstructural features of 304L austenitic stainless steel produced by wire-and-arc additive manufacturing. Int J Adv Manuf Technol 2020:3693–705. https://doi.org/10.1007/s00170-019-04868-8.
[37] Huang C, Kyvelou P, Zhang R, ben Britton T, Gardner L. Mechanical testing and microstructural analysis of wire arc additively manufactured steels. Mater Des 2022;216:110544. https://doi.org/10.1016/j.matdes.2022.110544.
[38] O. Belluzzi, Scienza delle Costruzioni, Zanichelli, 1946.
[39] Oerlikon, (n.d.). https://www.oerlikon.com/en/.
[40] Laghi V, Palermo M, Gasparini G, Girelli VA, Trombetti T. Experimental results for structural design of Wire-and-Arc Additive Manufactured stainless steel members. J Constr Steel Res 2020;167. https://doi.org/10.1016/j.jcsr.2019.105858.
[41] Kyvelou P, Slack H, Mountanou DD, Wadee MA, Britton TBen, Buchanan C, et al. Mechanical and microstructural testing of wire and arc additively manufactured sheet material. Mater Des 2020:108675. https://doi.org/10.1016/J.MATDES.2020.108675.
[42] Artec 3D webpage, (n.d.). https://www.artec3d.com.
[43] ISO, ISO 178: Plastics - Determination of flexural properties, (2010).
[44] Dassault Systemes, Abaqus CAE, (2016).
[45] W. Ramberg, W.R. Osgood, Description of stress-strain curves by three parameters, (1943).
[46] Gardner L, Nethercot DA. Numerical Modeling of Stainless Steel Structural ComponentsA Consistent Approach. J Struct Eng 2004;130:1586–601. https://doi.org/10.1061/(ASCE)0733-9445(2004)130:10(1586).
[47] European Committee for Standardization (CEN), EN 1993 1–4: Eurocode 3 - Design of steel structures, part 1–4: General rules, supplementary rules for stainless steel, (2015).